A Small-Baseline Approach for Investigating Deformations on Full-Resolution Differential SAR Interferograms

Ricardo Lanari, *Senior Member, IEEE*, Oscar Mora, *Member, IEEE*, Michele Manunta, Jordi J. Mallorquí, *Member, IEEE*, Paolo Berardino, and Eugenio Sansosti, *Senior Member, IEEE*

Abstract—This paper presents a differential synthetic aperture radar (SAR) interferometry (DIFSAR) approach for investigating deformation phenomena on full-resolution DIFSAR interferograms. In particular, our algorithm extends the capability of the small-baseline subset (SBAS) technique that relies on small-baseline DIFSAR interferograms only and is mainly focused on investigating large-scale deformations with spatial resolutions of about 100×100 m. The proposed technique is implemented by using two different sets of data generated at low (multilook data) and full (single-look data) spatial resolution, respectively. The former is used to identify and estimate, via the conventional SBAS technique, large spatial scale deformation patterns, topographic errors in the available digital elevation model, and possible atmospheric phase artifacts; the latter allows us to detect, on the full-resolution residual phase components, structures highly coherent over time (buildings, rocks, lava, structures, etc.), as well as their height and displacements. In particular, the estimation of the temporal evolution of these local deformations is easily implemented by applying the singular value decomposition technique. The proposed algorithm has been tested with data acquired by the European Remote Sensing satellites relative to the Campania area (Italy) and validated by using geodetic measurements.

Index Terms—Ground deformations, synthetic aperture radar (SAR), SAR interferometry.

I. INTRODUCTION

DIFFERENTIAL synthetic aperture radar (SAR) interferometry (DIFSAR) is a remote sensing technique that allows the investigaton of earth surface deformations with centimeter to millimeter accuracy, by exploiting the round-trip phase components of SAR images relative to an investigated area [1], [2]. Due to its capability to produce spatially dense deformation maps with no environmental impact on the investigated areas, this technique is becoming very important in civil protection scenarios. Moreover, the possibility to study the temporal evolution of the detected displacements is a key issue with important implications in the understanding of the dynamics of the deformation phenomena. An effective way to study this temporal behavior is the generation of deformation time-series; to do this, the information available from each interferometric data pair must be properly related to those included in the other acquisitions via the generation of an appropriate sequence of DIFSAR interferograms. In this context, several approaches, based on different interferometric combinations of the available SAR data relative to an investigated area, have been already proposed [3]–[9]. Among these procedures, the one referred to as the small-baseline subset (SBAS) approach [5] implements an ad hoc combination of the generated DIFSAR interferograms based on the following strategy. The data pairs used to produce the interferograms are characterized by a small spatial separation between the orbits (baseline), in order to limit spatial decorrelation effects. Moreover, the number of data acquisition used for the analysis is increased by properly *linking* independent SAR dataset separated by large baselines; this task is achieved by searching for the solution with a minimum kinetic energy, which is easily computed via the singular value decomposition (SVD) method.

The availability of both spatial and temporal information on the processed data is used to identify and filter out atmospheric phase artifacts; therefore, spatially dense deformation maps and, at the same time, deformation time-series for each investigated pixel of the imaged scene can be produced. The SBAS technique has already been successfully applied to investigate volcanic and tectonic related deformations [10]–[12]; however, because it was originally designed to monitor deformations occurring at a relatively large spatial scale (pixel dimensions of the order of 100×100 m are typical), it is not appropriate for analyzing local deformations that may affect, for example, single buildings or structures. Accordingly, we present in this paper a new algorithm that extends the monitoring capability of the SBAS technique to localize displacements by investigating full-resolution DIFSAR interferograms. The proposed solution, briefly described in [13], still relies on small-baseline interferograms but is implemented by using two different dataset generated at low (multilook data) and full (single-look data) spatial resolution, respectively. The former is used to identify, via the SBAS approach, large-scale deformation patterns, topographic errors in the available digital elevation model (DEM), and possible atmospheric phase artifacts; the latter is investigated after removing the low-resolution signal components; indeed, structures highly

R. Lanari, M. Manunta, P. Berardino, and E. Sansosti are with Istituto per il Rilevamento Elettromagnetico dell'Ambiente (IREA), National Research Council of Italy (CNR), 80124 Naples, Italy (e-mail: lanari.r@irea.cnr.it; manunta.m@irea.cnr.it; berardino.p@irea.cnr.it; sansosti.e@irea.cnr.it).

O. Mora is with Unitat de Teledetecció, Institut Cartogràfic de Catalunya, 08038 Barcelona, Spain (e-mail: omora@icc.es).

J. J. Mallorquí is with Universitat Politècnica de Catalunya (UPC), Signal Theory and Communication Department (TSC), 08034 Barcelona, Spain (e-mail: mallorqui@tsc.upc.es).

coherent over time (buildings, rocks, lava, structures, etc.) are identified on the residual phase signals jointly with an estimate of their local topography and of the mean velocity of the residual deformation. A final step, implemented via the SVD technique, leads to the estimation of the temporal evolution of the nonlinear components of the local displacement affecting these highly coherent structures. The availability of both deformation and topography information, at the two different spatial scales, allows us to exhaustively analyze the deformation behavior of the investigated pixels and to correctly localize them in a geographic (or cartographic) reference system.

We remark that the presented solution is easy to implement because it does not need any dedicated processing and can be used as a postprocessing step applied to a set of DIFSAR interferograms generated via already available interferometric data processing tools.

The proposed approach has been tested with a SAR dataset relative to the city of Naples, Italy, and surroundings, acquired by the European Remote Sensing (ERS) satellites. A validation of the results, via a comparison with leveling and gloabal positioning system (GPS) measurements, has been also carried out.

II. DIFSAR DATA ANALYSIS

A. Lowpass Signals

The presented approach relies on the availability of a set of $N+1$ SAR images of the same area acquired at the ordered times $(t_0, \ldots, t_N)$, from which a stack of single-look DIFSAR interferograms is produced. We consider here only interferometric data pairs with a small baseline, i.e., significantly smaller than the critical one [14].

Let us now assume, similarly to [5], that the DIFSAR stack is composed of M interferograms, with the following two index vectors:

$$\text{IS} = [\text{IS}_1, \ldots, \text{IS}_M] \quad \text{IE} = [\text{IE}_1, \ldots, \text{IE}_M] \qquad (1)$$

corresponding to the acquisition time-indexes associated with the image pairs used for the interferograms generation; in particular, we consider the master (IE) and slave (IS) images to be chronologically ordered, i.e., $t_{\text{IE}_m} > t_{\text{IS}_m} \; \forall m = 1, \ldots, M$. Accordingly, the phase expression for each pixel of the DIFSAR interferograms can be written as follows:

$$\delta\phi_m(x, r) = \phi(t_{\text{IE}_m}, x, r) - \phi(t_{\text{IS}_m}, x, r) \qquad (2)$$

where x and r are the azimuth and range pixel coordinates, $\phi(t_{\text{IE}_m}, x, r)$ and $\phi(t_{\text{IS}_m}, x, r)$ represent the phase values for the master and slave images, respectively, and $m = 1, \ldots, M$.

The first step of the procedure requires the evaluation of the spatially lowpass (LP) DIFSAR phase components, which may include large spatial scale deformation patterns, topographic errors caused by inaccuracies in the considered DEM, and possible contributions caused by atmospheric inhomogeneities between the acquisitions (often referred to as atmospheric phase artifacts). Because of the small-baseline characteristics of the interferograms, a complex (spatial) multilook operation can be easily applied to the DIFSAR data in order to get an estimate of

the LP signal component whose expression, for the mth interferogram, is [5], [8]

$$
\begin{aligned}
\delta\phi_m^{(\text{LP})}(x, r) \approx & \frac{4\pi}{\lambda} \left[d^{(\text{LP})}(t_{\text{IE}_m}, x, r) - d^{(\text{LP})}(t_{\text{IS}_m}, x, r) \right] \\
& + \frac{4\pi}{\lambda} \frac{b_m \, \Delta z^{(\text{LP})}(x, r)}{r \sin \vartheta} \\
& + \left[\phi_{\text{atm}}(t_{\text{IE}_m}, x, r) - \phi_{\text{atm}}(t_{\text{IS}_m}, x, r) \right] \\
& + \Delta n_m^{(\text{LP})}(x, r) \qquad (3)
\end{aligned}
$$

wherein $d^{(\text{LP})}(\cdot)$ and $\Delta z^{(\text{LP})}(\cdot)$ represent the LP components of the deformation signal and of the topographic errors, respectively, while the factor $\phi_{\text{atm}}(t_{\text{IE}_m}, x, r) - \phi_{\text{atm}}(t_{\text{IS}_m}, x, r)$ accounts for possible atmospheric phase artifacts and $\Delta n_m^{(\text{LP})}(\cdot)$ for the noise contributions. Moreover, λ represents the transmitted signal wavelength, b_m the perpendicular baseline component, and ϑ the incidence angle. We further remark that we assume hereafter $d^{(\text{LP})}(t_0, x, r) \equiv 0 \; \forall(x, r) \in D$, being D the investigated domain; therefore, it is natural to identify $d^{(\text{LP})}(t_n, x, r)$ with $n = 0, \ldots, N$, as the LP deformation time-series relevant to the pixel located at (x, r) and computed with respect to the reference acquisition time t_0.

Based on (3), the conventional SBAS approach can be applied to single out, for each coherent pixel, the signal components $\Delta z^{(\text{LP})}(x, r)$ and $d^{(\text{LP})}(t_n, x, r) \; \forall n = 0, \ldots, N$. To achieve this task, possible atmospheric artifacts are identified and compensated for by applying the three-dimensional (space-time) filtering step described in [5], which is based on the analysis shown in [3] and [15]; however, alternative filtering approaches, such as the one discussed in [8] and [9], can be also included with no significant impact on the implementation of the processing chain.

As a final remark, we underline that some concerns on the correctness of the solution provided by the SBAS technique [5] have been recently raised in [7]. We stress that these concerns are based on a single unrealistic example; therefore, we present in the Appendix an error analysis based on a number of simulated experiments that demonstrate the effectiveness of the approach in real scenarios.

B. Highpass Signals

Let us now focus on the full-resolution DIFSAR data that are considered, in our approach, after the modulo-2π subtraction of the LP components; because of this phase removal step, the obtained residual phase pattern will be related to the highpass (HP) deformation and topographic phase signals, the former also referred in the following to as *residual deformations* (the HP contributions will be often referred in the following to as high-frequency or high-resolution signal components). In particular, the residual phase of each pixel within the mth single-look interferogram can be expressed as follows:

$$
\begin{aligned}
\delta\phi_m^{(\text{HP})}(x, r) = & \frac{4\pi}{\lambda} \left[(t_{\text{IE}_m} - t_{\text{IS}_m}) \, v^{(\text{HP})}(x, r) \right. \\
& \left. + \beta^{(\text{HP})}(t_{\text{IE}_m}, x, r) - \beta^{(\text{HP})}(t_{\text{IS}_m}, x, r) \right] \\
& + \frac{4\pi}{\lambda} \frac{b_m \Delta z^{(\text{HP})}(x, r)}{r \sin \vartheta} + \Delta n_m^{(\text{HP})}(x, r) \quad (4)
\end{aligned}
$$

wherein $v^{(\text{HP})}(\cdot)$ and $\beta^{(\text{HP})}(\cdot)$ represent the mean velocity and the nonlinear component of the residual displacement,

respectively, $\Delta z^{(\mathrm{HP})}(\cdot)$ the high-resolution topographic error, and $\Delta n_m^{(\mathrm{HP})}(\cdot)$ the noise component.

Some considerations on (4) are in order. First of all, we remark that the atmospheric phase artifacts are pertinent of the LP DIFSAR components only. This occurs because the LP filtering operation is carried out with a filter whose bandwidth is chosen, both in azimuth and range, significantly larger than that of the atmospheric phase signal, whose spatial correlation length is typically of about 1 km [15]. Accordingly, the atmospheric phase artifacts do not affect the HP signal components.

Moreover, we stress that only a wrapped measurement of the signal $\delta\phi_m^{(\mathrm{HP})}(\cdot)$ [see (4)] is available after the above-mentioned modulo 2π subtraction; accordingly, a signal decoupling into a linear and a nonlinear component has been considered in (4) in order to implement the residual phase-unwrapping operation. In particular, the following two-step unwrapping strategy is considered; first, we estimate the terms $v^{(\mathrm{HP})}(\cdot)$ and $\Delta z^{(\mathrm{HP})}(\cdot)$ in (4) that maximize the temporal coherence factor

$$\gamma^{(\mathrm{HP})}(x,r) = \frac{1}{M}\left|\sum_{m=1}^{M}\exp\left[j\left(\delta\phi_m^{(\mathrm{HP})}(x,r)\right. \right.\right.$$
$$\left.\left.\left. - \delta\phi_m^{(\mathrm{model})}(x,r)\right)\right]\right| \quad (5)$$

wherein $\delta\phi_m^{(\mathrm{model})}(x,r)$ represents the phase model assumed as

$$\delta\phi_m^{(\mathrm{model})}(x,r) = \frac{4\pi}{\lambda}\left(t_{\mathrm{IE}_m} - t_{\mathrm{IS}_m}\right)v^{(\mathrm{HP})}(x,r)$$
$$+ \frac{4\pi}{\lambda}\frac{b_m \Delta z^{(\mathrm{HP})}(x,r)}{r\sin\vartheta}. \quad (6)$$

Note that the temporal coherence factor in (5) provides a quantitative measurement of the degree of similarity between the HP deformation signal and the assumed model (6). The second step consists (for pixels exhibiting a coherence value larger than a fixed threshold) of the determination of the nonlinear deformation component $\beta^{(\mathrm{HP})}(\cdot)$ in (4). To this end, we assume that the deviation of the model from the true HP component of the phase signal is within the $(-\pi, +\pi)$ interval. Therefore, we can obtain a relationship between the HP phase signal and the nonlinear component of the residual deformation by simply subtracting, modulo-2π, the estimated model (6) from the signal in (4). This operation leads to the system (7), shown at the bottom of the page, where the $\langle\cdot\rangle_{2\pi}$ symbol represents the modulo-2π operation. Clearly, the known term at the right-hand side of (7) is an estimate of the unwrapped difference if the quoted hypothesis is verified.

The $\beta^{(\mathrm{HP})}(\cdot)$ components can be now achieved by inverting the system (7) that, however, exhibits a smaller number of independent equations than unknowns if more than one subset is present. In this case, the system has a rank deficiency; thus, even the least squares (LS) solution is not unique, and additional constraints are necessary. The use of the SVD method allows us to compute, among all the LS solutions, the one with minimum length (norm) [16]; in this case, the solution is robust with respect to the noise effects and unwrapping errors and allows us to effectively combine the information available from the different subset. In analogy to [5], we rewrite the system (7) in terms of velocities, by replacing the unknowns $\beta^{(\mathrm{HP})}(\cdot)$ with the components of the velocity vector in (8), shown at the bottom of the page.

Based on (8), we may now rewrite (7) as the system (9), shown at the bottom of the page, which can be solved via the SVD method to compute the velocity vector in (8). We remark that in this case the minimum norm constraint is relevant to the $\underline{v}_{\mathrm{nonlinear}}^{(\mathrm{HP})}(\cdot)$ vector and allows us to avoid large discontinuities in the final solution, as discussed in [5]. Of course, in this case an additional, but trivial, integration operation [see (9)] is necessary to recover $\beta^{(\mathrm{HP})}(\cdot)$ from the computed $\underline{v}_{\mathrm{nonlinear}}^{(\mathrm{HP})}(\cdot)$ signal.

$$\begin{cases} \frac{4\pi}{\lambda}\left[\beta^{(\mathrm{HP})}\left(t_{\mathrm{IE}_1},x,r\right) - \beta^{(\mathrm{HP})}\left(t_{\mathrm{IS}_1},x,r\right)\right] + \Delta n_1^{(\mathrm{HP})}(x,r) = \left\langle\delta\phi_1^{(\mathrm{HP})} - \delta\phi_1^{(\mathrm{model})}\right\rangle_{2\pi} \\ \frac{4\pi}{\lambda}\left[\beta^{(\mathrm{HP})}\left(t_{\mathrm{IE}_2},x,r\right) - \beta^{(\mathrm{HP})}\left(t_{\mathrm{IS}_2},x,r\right)\right] + \Delta n_2^{(\mathrm{HP})}(x,r) = \left\langle\delta\phi_2^{(\mathrm{HP})} - \delta\phi_2^{(\mathrm{model})}\right\rangle_{2\pi} \\ \vdots \\ \frac{4\pi}{\lambda}\left[\beta^{(\mathrm{HP})}\left(t_{\mathrm{IE}_M},x,r\right) - \beta^{(\mathrm{HP})}\left(t_{\mathrm{IS}_M},x,r\right)\right] + \Delta n_M^{(\mathrm{HP})}(x,r) = \left\langle\delta\phi_M^{(\mathrm{HP})} - \delta\phi_M^{(\mathrm{model})}\right\rangle_{2\pi} \end{cases} \quad (7)$$

$$\underline{v}_{\mathrm{nonlinear}}^{(\mathrm{HP})}(x,r)^T = \left[v_1 = \frac{\beta^{(\mathrm{HP})}(t_1,x,r) - \beta^{(\mathrm{HP})}(t_0,x,r)}{t_1 - t_0}, \ldots, v_{M-1} = \frac{\beta^{(\mathrm{HP})}\left(t_{M-1},x,r\right) - \beta^{(\mathrm{HP})}\left(t_{M-2},x,r\right)}{t_{M-1} - t_{M-2}}\right] \quad (8)$$

$$\begin{cases} \sum_{k=\mathrm{IS}_1+1}^{\mathrm{IE}_1}(t_k - t_{k-1})v_k + \Delta n_1^{(\mathrm{HP})}(x,r) = \left\langle\delta\phi_1^{(\mathrm{HP})} - \delta\phi_1^{(\mathrm{model})}\right\rangle_{2\pi} \\ \sum_{k=\mathrm{IS}_1+1}^{\mathrm{IE}_1}(t_k - t_{k-1})v_k + \Delta n_2^{(\mathrm{HP})}(x,r) = \left\langle\delta\phi_2^{(\mathrm{HP})} - \delta\phi_2^{(\mathrm{model})}\right\rangle_{2\pi} \\ \vdots \\ \sum_{k=\mathrm{IS}_M+1}^{\mathrm{IE}_M}(t_k - t_{k-1})v_k + \Delta n_M^{(\mathrm{HP})}(x,r) = \left\langle\delta\phi_M^{(\mathrm{HP})} - \delta\phi_M^{(\mathrm{model})}\right\rangle_{2\pi} \end{cases} \quad (9)$$
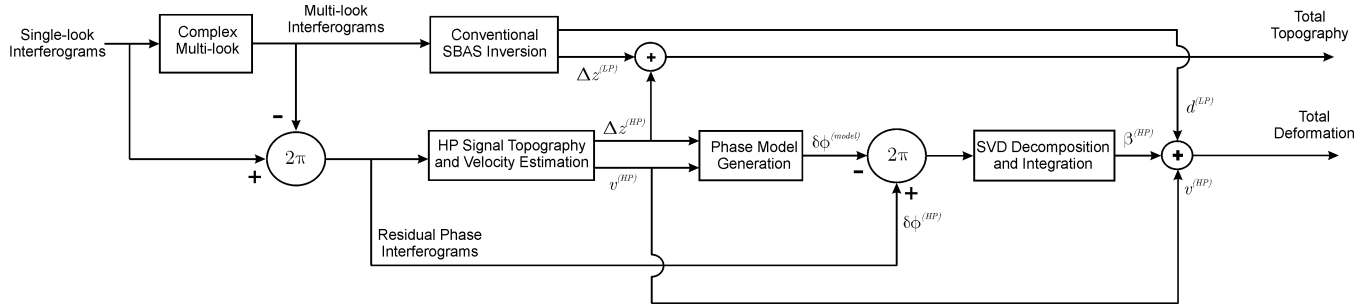
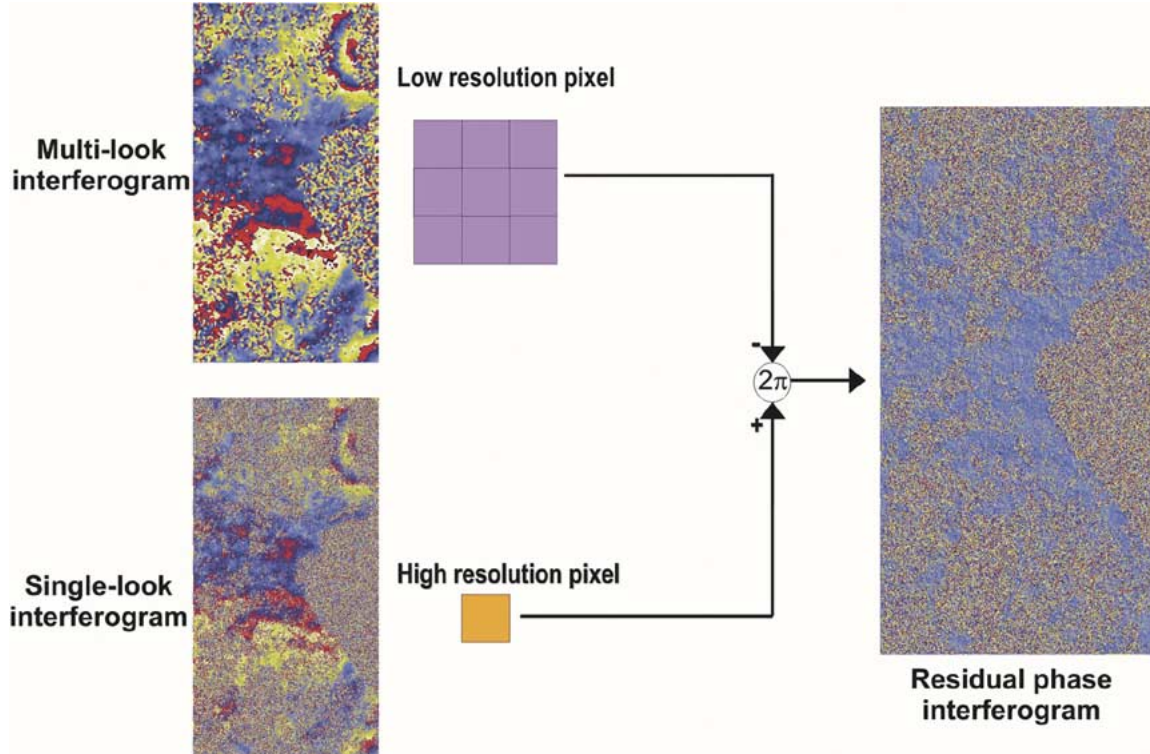Fig. 1.   Block diagram of the implemented procedure.

Fig. 2.   Pictorial example of the lowpass/highpass DIFSAR signal decoupling.

At this stage, the overall deformation signal can be finally computed by combining the linear and nonlinear HP displacements computed from the residual DIFSAR phase [see (4)] and the large spatial scale displacements estimated from the multilook signals [see (3)]; accordingly, the overall deformation signal expression is represented by

$$d(t_n, x, r) = d^{(\mathrm{LP})}(t_n, x, r)$$
$$+ (t_n - t_0)v^{(\mathrm{HP})}(x, r) + \beta^{(\mathrm{HP})}(t_n, x, r) \quad (10)$$

$\forall n = 0, \ldots, N$, while the estimated topographic contribution can be equivalently recovered as

$$\Delta z(x, r) = \Delta z^{(\mathrm{LP})}(x, r) + \Delta z^{(\mathrm{HP})}(x, r). \quad (11)$$

Few final remarks on the presented analysis are in order. First of all, we want to stress that the deformation signal decoupling into a linear and a nonlinear component [see (4)] is similar to what has been implemented in the permanent scatterers (PS) approach [3], [4]; however, we also underline that, unlike the PS technique, the discussed inversion procedure is applied to the residual phase

signal components only because an LP signal removal step, which includes the atmospheric phase components, has been previously applied; for this reason the overall analysis is carried out on the phase signal relevant to single pixels instead of the phase differences between neighboring pixels. In this context, the quasi-linear model assumption (6) is certainly meaningful.

III. ALGORITHM DESCRIPTION

The overall processing procedure is implemented according to the block diagram of Fig. 1, wherein the input data consists of a stack of single-look complex DIFSAR interferograms computed from small-baseline SAR data pairs. The starting point of the procedure is represented by the DIFSAR signal decoupling into LP and HP components. The former are obtained by implementing a complex multilook operation, the latter by subtracting, modulo-2π the obtained LP signals from the high-resolution data; a pictorial example of the LP/HP signal decoupling is shown in Fig. 2. We remark that the LP filtering step is carried out via an average operation with a data window

of length of about 100 m in both azimuth and range directions, thus certainly smaller than the spatial correlation of the atmospheric phase artifacts [15]. The LP data processing is finalized by the application of the conventional SBAS technique [5] that allows us to recover the deformation signal and the errors in the available DEM and, at the same time, to detect and filter out possible atmospheric phase artifacts.

Regarding the HP signal estimation, the data processing implementation follows the lines of the analysis presented in the previous section. In particular, we first compute the high-resolution terms $v^{(HP)}(\cdot)$ and $\Delta z^{(HP)}(\cdot)$ in (6) via the maximization of the coherence factor $\gamma^{(HP)}(\cdot)$; then, on the pixels with a coherence value larger than a chosen threshold, we recover the nonlinear HP signal component via the SVD-based inversion of (9), followed by the integration of the estimated $\underline{v}^{(HP)}_{\text{nonlinear}}(\cdot)$ vector [see (8)]. At this processing stage, both low- and high-resolution topography and deformation information are available; the former are essential to correctly geolocate the detected coherent pixels, i.e., to estimate their positions in a selected reference system; the latter allow us to fully analyze the observed deformation behavior.

As a final remark, we note that the considered processing strategy requires the investigated areas to be coherent both at low and high resolution. This may be not the case in presence of isolated structures or for areas at the edge of low-resolution coherent zones, where no LP information is available. Accordingly, a further operation is required in order to detect and analyze these targets. In this case, pixels with a temporal coherence value significantly lower than the selected threshold, and located in incoherent zones of the multilook interferograms, are reconsidered. In particular, we investigate pixels with a temporal coherence value larger than 0.35 but highly correlated with targets located in the surrounding areas, where the overall processing has been already successfully carried out. In this case, the data processing is identical to the one carried out in previous HP data processing step, with the only difference that the residual phase of the investigated pixel is computed by subtracting the HP and LP signal components relative to the adjacent coherent pixels detected in the surrounding areas. Following this operation, not reported in Fig. 1 for sake of simplicity, only those pixels with an achieved high temporal coherence value will be assumed reliable and considered in the final output.

IV. EXPERIMENTAL RESULTS

The validation of the proposed approach has been carried out by processing a dataset of 55 ERS-1/ERS-2 images acquired on descending orbits and spanning the time interval from June 1992 to September 2001 (see Table I). Based on this dataset, 138 DIFSAR interferograms, with a maximum baseline of about 130 m, have been computed. The investigated area is centered on the city of Naples (see Fig. 3) and includes the Campi Flegrei caldera (left) and the Somma-Vesuvius volcanic complex (right). In order to provide an overall picture of the detected large-scale deformations, we present in Fig. 3 the false-color map showing the cumulative deformation measured, for each investigated pixel, in the considered time interval. Fig. 3 clearly

TABLE I
ERS-1/2 DATASET. DIFFERENT SUBSETS ARE
HIGHLIGHTED IN THE LAST COLUMN

Mission	Orbit	Day	Month	Year	b	SB Subset
ERS1	4690	8	6	1992	99	1
ERS1	6694	26	10	1992	-24	1
ERS1	7195	30	11	1992	258	1
ERS1	8197	8	2	1993	-445	2
ERS1	8698	15	3	1993	-20	1
ERS1	9700	24	5	1993	-418	2
ERS1	10201	28	6	1993	-492	2
ERS1	10702	2	8	1993	-18	1
ERS1	11203	6	9	1993	130	1
ERS1	12205	15	11	1993	-41	1
ERS1	19563	12	4	1995	-425	2
ERS1	21066	26	7	1995	-50	1
ERS2	1393	27	7	1995	-85	1
ERS2	1894	31	8	1995	-456	2
ERS2	2395	5	10	1995	572	3
ERS2	3397	14	12	1995	118	1
ERS1	24072	21	2	1996	519	3
ERS2	4399	22	2	1996	574	3
ERS2	4900	28	3	1996	-1029	4
ERS1	25074	1	5	1996	499	3
ERS2	5401	2	5	1996	409	3
ERS2	5902	6	6	1996	-1005	4
ERS2	6904	15	8	1996	-447	2
ERS2	7906	24	10	1996	470	3
ERS2	8407	28	11	1996	703	3
ERS2	8908	2	1	1997	-288	2
ERS2	9409	6	2	1997	0	1
ERS2	10411	17	4	1997	314	3
ERS2	10912	22	5	1997	-330	2
ERS2	11914	31	7	1997	-293	2
ERS2	13417	13	11	1997	-430	2
ERS2	13918	18	12	1997	-372	2
ERS2	14920	26	2	1998	-1375	5
ERS2	15922	7	5	1998	252	3
ERS2	16423	11	6	1998	563	3
ERS2	16924	16	7	1998	-965	4
ERS2	17926	24	9	1998	31	1
ERS2	20431	18	3	1999	-151	1
ERS2	21934	1	7	1999	-78	1
ERS2	22435	5	8	1999	-92	1
ERS2	22936	9	9	1999	-873	4
ERS2	23437	14	10	1999	-518	2
ERS2	24439	23	12	1999	-374	2
ERS2	24940	27	1	2000	-331	2
ERS2	25441	2	3	2000	-887	4
ERS2	26443	11	5	2000	713	3
ERS2	26944	15	6	2000	-398	2
ERS2	27445	20	7	2000	-829	4
ERS2	27946	24	8	2000	263	3
ERS2	28447	28	9	2000	-157	1
ERS2	28948	2	11	2000	-441	2
ERS2	29449	7	12	2000	-1352	5
ERS2	29950	11	1	2001	-84	1
ERS2	32956	9	8	2001	581	3
ERS2	33457	13	9	2001	-49	1

shows that a very significant deformation phenomenon is affecting the Campi Flegrei caldera area with displacements exceeding, in some zones, 20 cm [11]; moreover, a deformation
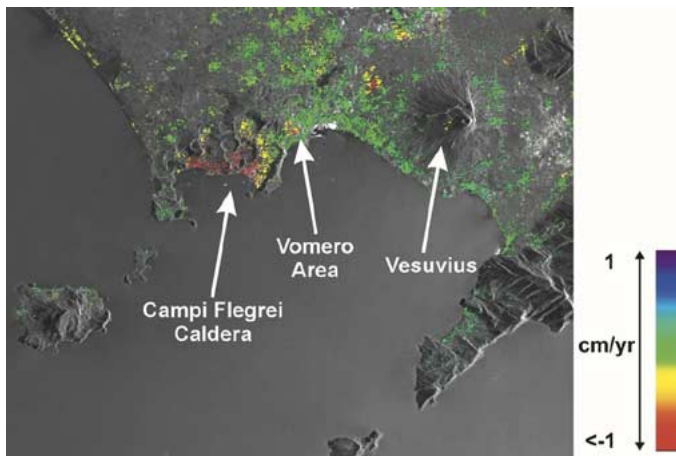
Fig. 3. Multilook SAR image of the city of Naples and surroundings. The superimposed false-color map is relevant to the cumulative deformation estimated in the time interval June 1992 to September 2001. The Campi Flegrei caldera, the Vesuvius volcano, and the Vomero zone, within the city of Naples, have been highlighted. Note that, for visualization purposes only, a color scale saturation has been applied.

effect is clearly visible in the urban area of Naples also; this phenomenon is rather localized and mostly affects the Vomero area with a maximum deformation of about 6 cm [17], [18]. Finally, we also remark the very peculiar pattern of deformation affecting the top of the Vesuvius volcano and, particularly, an area around its base with the terrain subsidence reaching in some cases about 7 cm [10]. As an additional remark, we underline that areas where the measurement accuracy is affected by decorrelation noise have been excluded from the false-color map of Fig. 3.

In order to investigate the capability of the proposed approach and to analyze deformations at full-resolution scale, we focused our analysis on the Vomero and Campi Flegrei areas; the reason of this selection is twofold. First of all, they are highly urbanized zones; therefore it can be relevant to have a figure of the deformations affecting single buildings and structures. Moreover, geodetic information are available in these two areas; therefore, a DIFSAR/geodetic data comparison can be carried out. To give an idea of the pixel density distribution in the Vomero zone, let us first show, in Fig. 4, the map of the coherent points that has been detected, geolocated, and overlaid to an optical image of the investigated area. Note that in this zone the density of coherent points [coherence larger than 0.7; see (5)] is about 250 points/km^2; moreover, the false-color representation in Fig. 4 provides information about the mean deformation velocity of the investigated targets. By inspecting Fig. 4 and its zoomed window in Fig. 5, it is evident that the deformations of several structures and buildings can be investigated. In particular, we have considered the coherent pixel highlighted in Fig. 5, which is relevant to a building where a leveling benchmark is located; therefore, several measurements are available starting from 1995. The result of the comparison between DIFSAR and geodetic displacement is shown in the plot of Fig. 5, wherein the leveling data have been projected on the radar line of sight (LOS). The good agreement between the SAR (triangles) and the leveling (stars) data is evident;

Fig. 4. Full-resolution coherent pixel (circles) map superimposed to an optical image of the Vomero zone (courtesy of CIRAM). The false-color representation within the circles is relative to the estimated deformation mean velocity expressed in centimeters per year.
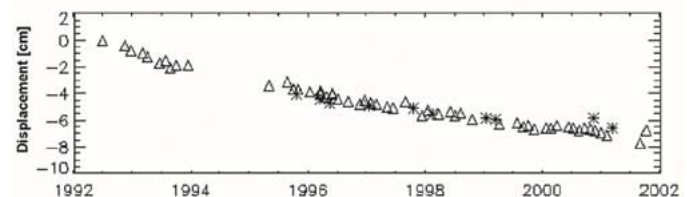

Fig. 5. Comparison between leveling (stars) and DIFSAR (triangles) deformation time-series relevant to a building (identified by the white arrow) located in the maximum deformation area of the Vomero zone, shown in the picture.
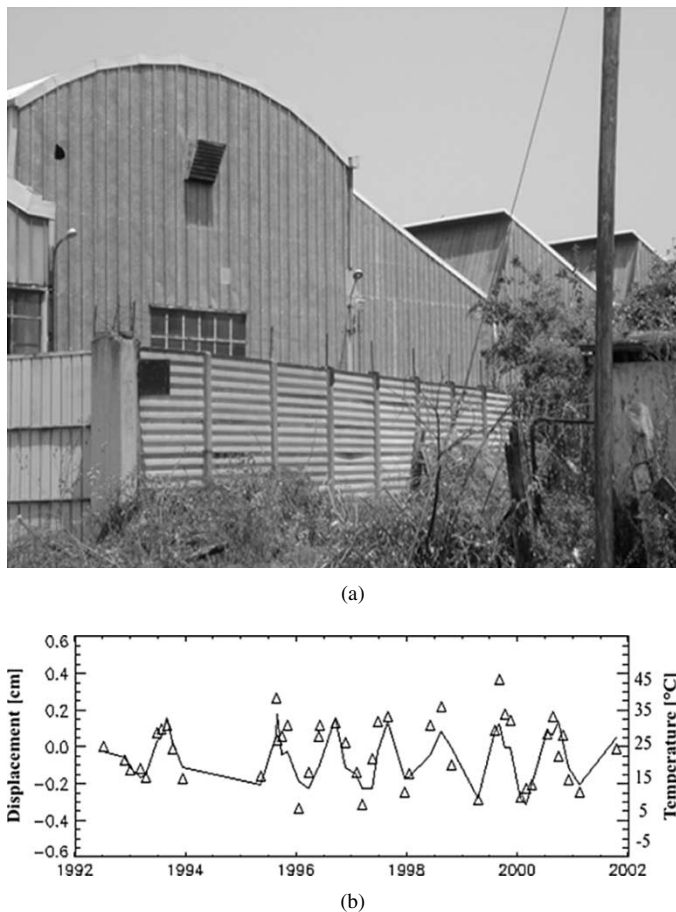
(a)

(b)

Fig. 6.   (a) Picture of an investigated metallic structure located in the urban area of Naples. (b) Comparison between the measured DIFSAR displacements (triangles) and the measured temperatures (continuous line) ranging in the interval (6, 33) Celsius degrees.

indeed, the standard deviation of the difference between the two measurements is less than 5 mm, while the mean value is practically negligible.

As additional experiments, we have correlated the DIFSAR displacements with the temperatures measured on the ground at the same time of the ERS acquisitions. Based on this analysis, we have identified several structures showing high correlation values (larger than 0.8), and we have verified that these targets are mostly represented by metallic structures. As an example, we present in Fig. 6(a) the picture of one of these buildings and in Fig. 6(b) the comparison between the measured deformation time-series and the corresponding values obtained directly from the temperatures at the ERS acquisition times. Again, the agreement between the two different measurements is good. Also, in this case, a quantitative comparison has been performed by considering a linear dilatation model; this analysis shows that the difference has a negligible mean value and a standard deviation of about 0.9 mm. Obviously, the presented technique does not allow us to automatically discriminate between thermal deformations and other kind of localized displacements; however, it is also evident that the thermal effects can be reasonably detected by observing if the deformations have a seasonal behavior.

Additional experiments have been carried out in the Campi Flegrei area; in this case, the map of the detected coherent pixels,
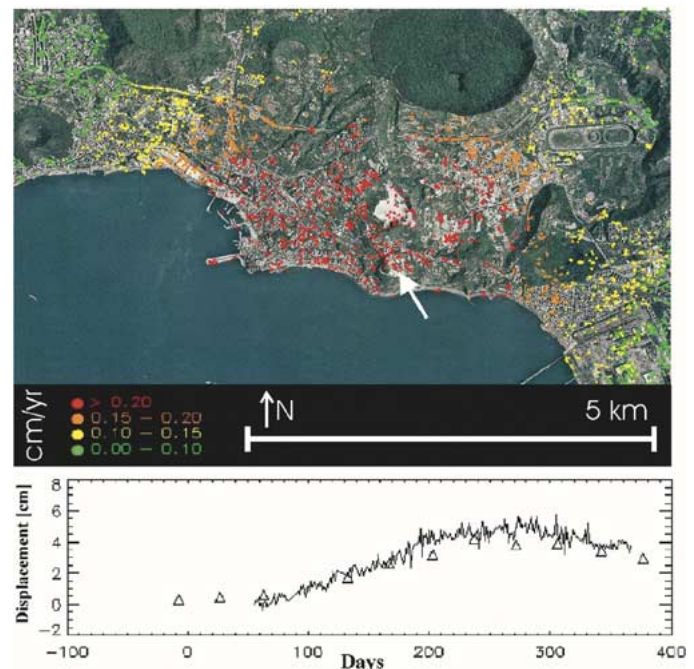

Fig. 7.   Full-resolution coherent pixel map superimposed to an optical image of the Campi Flegrei zone. The presented plot shows the comparison, on a selected site identified by the white arrow, between GPS (continuous line) and DIFSAR (triangles) time-series. The zero of the horizontal axis corresponds to January 1, 2000. Starting date of the GPS acquisition is at the beginning of March 2000.

overlaid to an optical image of the area, is shown in Fig. 7. Also, in this case, a quantitative experiment has been performed. In particular, we compared the SAR displacements with the continuous GPS measurements carried out, during year 2000, at a site located in the highlighted zone of Fig. 7; again, the good agreement between the DIFSAR and the LOS projected GPS deformations is evident; in this case, the difference has a mean value of 1 mm and a standard deviation of about 6 mm.

As a final step, we have investigated the capability of the approach to estimate the full-resolution topography, which is needed for a precise geocoding of the DIFSAR products. Fig. 8(a) and (b) shows, as an example, the location of the detected coherent pixels relevant to the San Paolo stadium without and with the estimated topographic information shown in (11), respectively. The impact of this correction is evident, and it is crucial to identify the investigated structures as well as to integrate the DIFSAR data in a geographic information system [18].

V. DISCUSSION AND CONCLUSION

This paper describes a new approach for investigating the temporal evolution of deformation phenomena on full-resolution DIFSAR interferograms. To achieve this task, we have extended the SBAS approach [5] that was originally developed for low-resolution DIFSAR data analysis. The proposed solution retains the small-baseline constraint on the processed interferograms but is implemented by using single-look and multilook data. The presented results, achieved on an ERS-1/2 dataset, have been successfully validated via a comparison with GPS and leveling data.

Fig. 8.   Location of the coherent pixels relative of the San Paolo Stadium(a) without and (b) with topographic correction shown in (11). An optical image of the stadium is on the background.
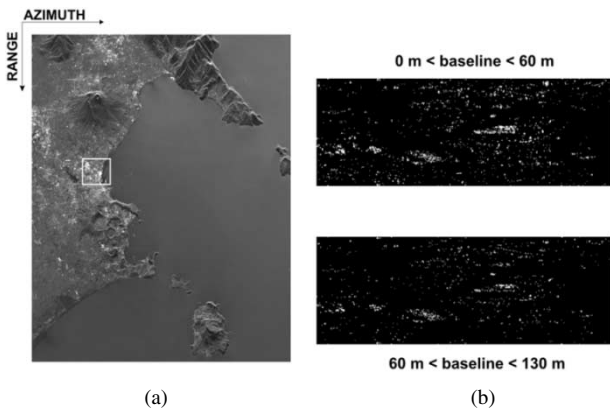

Fig. 9.   (a) Multilook SAR image of the city of Naples and surroundings, wherein the investigated test area is highlighted. (b) Detected coherent pixels on the interferograms (upper) with a baseline smaller than 60 m and (lower) with a baseline value between 60–130 m.

One important question that may arise by considering the proposed results is to assess whether the detected high-resolution coherent pixels are dependent or not on the baseline constraint; in other words, whether the use of small-baseline interferograms produces different results with respect to an analysis based, for instance, also on large baseline interferograms. This issue is worth for an extended analysis that is outside the scope of this paper. However, in order to provide a contribution, although partial, to the comprehension of this point, we have carried out a simple experiment. In particular, we have divided the produced DIFSAR interferograms in two datasets including interferograms with a baseline smaller than 60 m (69 interferograms) and between 60–130 m (69 interferograms), respectively. The extended SBAS approach has been applied to both datasets, and a comparison has been carried out with respect to the number of detected coherent structures; in this case, the selected test area is the one highlighted in Fig. 9(a), which has been chosen because of the high density of the coherent pixels. By considering the

test results, it comes out that the number of coherent pixels in the two datasets is not the same, and in particular, it results that the baseline increase corresponds to a decrease of the number of coherent structures, which in our case is quantified in about 40% [Fig. 9(b)].

Based on this preliminary result, it seems that there is a dependence of the number of coherent pixels with respect to the DIFSAR baseline. Accordingly, the selection of a baseline constraint may represent a relevant parameter if, for instance, a maximization of the coherent pixel density is required. In any case, a more detailed analysis on this matter is essential for fully assessing this relevant issue.

APPENDIX

We present in the following an error analysis that is relevant to the application of the SVD method within the SBAS approach. Because an analytical formulation of these errors is practically untreatable, we prefer to focus on simulated experiments carried out by considering different displacement models and a real SAR data acquisition configuration that in our case is the one considered in the experimental Section IV and described in Table I. As a first example, we have simulated, similarly to that in [7], a linear deformation signal [see Fig. 10(a)] with a variation of 10 cm within the considered ten-year time interval. The SVD reconstruction error is presented in Fig. 10(b); note that, as expected, we have no error (zero or constant values) for data belonging to a single subset; indeed, the SVD only introduces small offsets among the considered SBAS leading to a maximum error of submillimetric order (less than 0.4 mm), thus significantly smaller than that related to other possible sources such as decorrelation noise, phase-unwrapping errors, etc.

Furthermore, we have considered the deformation signal presented in Fig. 11(a) that mimics a real deformation behavior; in particular, it is pertinent to the maximum displacement zone in
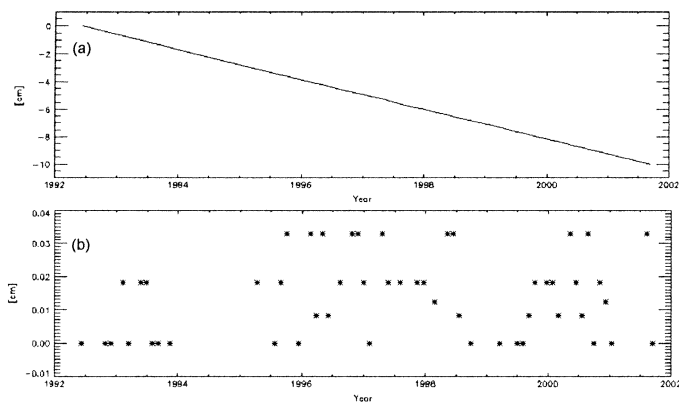
Fig. 10. (a) Simulated linear deformation model. (b) Difference between the retrieved signal and the model.
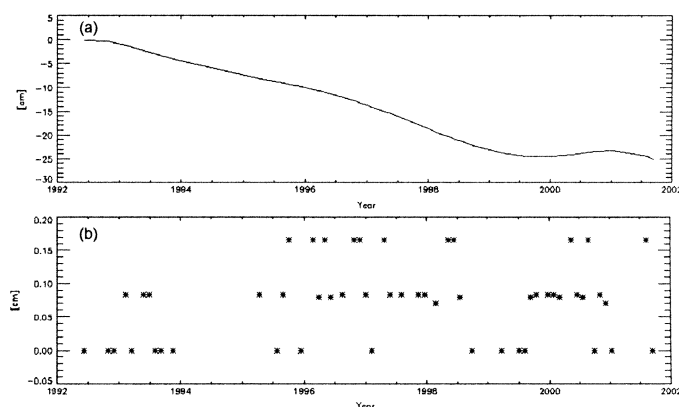

Fig. 11. (a) Simulated deformation model that mimics the deformation behavior of the maximum displacement zone in the Campi Flegrei volcanic area [11]. (b) Difference between the retrieved signal and the model.
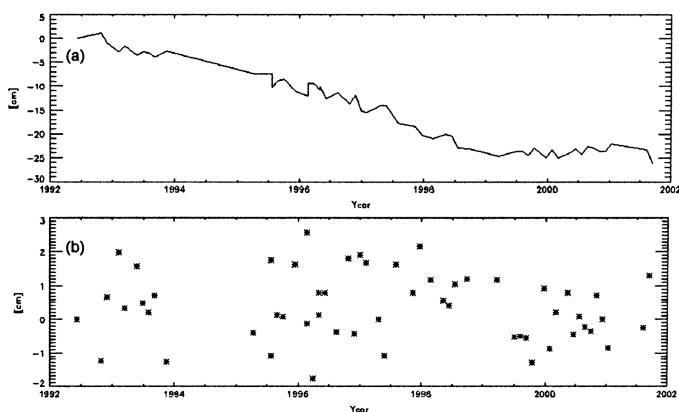

Fig. 12. (a) Simulated deformation model obtained by addying to the model of Fig. 11(a) a uniformly distributed random noise with 1-cm standard deviation. (b) Difference between the retrieved signal and the model of Fig. 11(a).

the Campi Flegrei volcanic area [11]. The corresponding reconstruction error, which is shown in Fig. 11(b), presents a maximum amplitude value, which is smaller than 2 mm.

Let us now investigate the impact of noise. Accordingly, we have added to the model of Fig. 11(a) a uniformly distributed random noise with 1-cm standard deviation: the perturbed model is plotted in Fig. 12(a). The difference between the

SVD-based reconstruction and the original signal of Fig. 11(a) is shown in Fig. 12(b). In this case, we have verified that the measured difference still exhibits a standard deviation of the order of 1 cm; this clearly shows that the SBAS procedure does not introduce any significant additional noise.

We believe that the presented examples demonstrate the effectiveness of the SBAS approach; moreover, we remark that the presented results are not a consequence of the selected data acquisition configuration; indeed, similar results, not reported here for brevity, have been also obtained with alternative configurations. On the contrary, we stress that the errors reported in [7] are the consequence of a nonrealistic example, wherein only six acquisitions were considered (no significant time-series involves less than 20/30 images), divided in two subset of three acquisition each. Last but not least, the six data considered in [7] have nearly no temporal overlap, while it is evident that only a significant temporal interleaving may provide a robust *linking* among the different subsets, no matter which technique is used to achieve this task.

REFERENCES

[1] K. Gabriel, R. M. Goldstein, and H. A. Zebker, "Mapping small elevation changes over large areas: Differential interferometry," *J. Geophys. Res.*, vol. 94, pp. 9183–9191, 1989.
[2] D. Massonnet, M. Rossi, C. Carmona, F. Ardagna, G. Peltzer, K. Feigl, and T. Rabaute, "The displacement field of the Landers earthquake mapped by radar interferometry," *Nature*, vol. 364, pp. 138–142, 1993.
[3] A. Ferretti, C. Prati, and F. Rocca, "Nonlinear subsidence interferometry," *IEEE Trans. Geosci. Remote Sensing*, vol. 38, pp. 2202–2212, Sept. 2000.
[4] ——, "Permanent scatterers in SAR interferometry," *IEEE Trans. Geosci. Remote Sensing*, vol. 39, pp. 8–20, Jan. 2001.
[5] P. Berardino, G. Fornaro, R. Lanari, and E. Sansosti, "A new algorithm for surface deformation monitoring based on small baseline differential SAR interferograms," *IEEE Trans. Geosci. Remote Sensing*, vol. 40, pp. 2375–2383, Nov. 2002.
[6] M. Costantini, F. Malvarosa, F. Minati, and L. Pietranera, "Optimal combination of multiple SAR differential interferometric measurements for monitoring terrain displacements," in *Proc. IEEE/ISPRS Joint Workshop*, 2001, pp. 53–57.
[7] S. Usai, "A least-squares database approach for SAR interferometric data," *IEEE Trans. Geosci. Remote Sensing*, vol. 41, pp. 753–760, Apr. 2003.
[8] O. Mora, J. J. Mallorquí, and A. Broquetas, "Linear and nonlinear terrain deformation maps from a reduced set of interferometric SAR images," *IEEE Trans. Geosci. Remote Sensing*, vol. 41, pp. 2243–2253, Oct. 2003.
[9] O. Mora, J. J. Mallorquí, and J. Duro, "Generation of deformation maps at low resolution using differential interferometric SAR data," in *Proc. IGARSS*, vol. 5, 2002, pp. 2696–2698.
[10] R. Lanari, G. De Natale, P. Berardino, E. Sansosti, G. P. Ricciardi, S. Borgstrom, P. Capuano, F. Pingue, and C. Troise, "Evidence for a peculiar style of ground deformation inferred at Vesuvius volcano," *Geophys. Res. Lett.*, vol. 29, no. 9, 2002.
[11] R. Lanari, P. Berardino, S. Borgstrom, C. Del Gaudio, P. De Martino, G. Fornaro, S. Guarino, G. P. Ricciardi, E. Sansosti, and P. Lundgren, "The use of IFSAR and classical geodetic techniques in civil protection scenarios: Application to the Campi Flegrei uplift event of 2000," *J. Volcanol. Geotherm. Res.*, vol. 133, no. 1–4, pp. 247–280, May 2004.

IEEE TRANSACTIONS ON GEOSCIENCE AND REMOTE SENSING, VOL. 42, NO. 7, JULY 2004

[12] P. Lundgren, F. Casu, M. Manzo, A. Pepe, P. Berardino, E. Sansosti, and R. Lanari, "Gravity and magma induced spreading of Mount Etna volcano revealed by satellite radar interferometry," *Geophys. Res. Lett.*, vol. 31, no. 4, Feb. 17, 2004. DOI:10.1029/2003GL018736.

[13] R. Lanari, O. Mora, M. Manunta, J. J. Mallorquí, P. Berardino, S. Guarino, G. Zeni, A. Pepe, and E. Sansosti, "A differential SAR interferometry approach for monitoring urban deformation phenomena," in *Proc. URBAN 2003, GRSS/ISPRS Joint Workshop*, Berlin, Germany, 2003, pp. 57–61.

[14] H. A. Zebker and J. Villasenor, "Decorrelation in interferometric radar echoes," *IEEE Trans. Geosci. Remote Sensing*, vol. 30, pp. 950–959, Sept. 1992.

[15] R. Hanssen, *Radar Interferometry*. Amsterdam, The Netherlands: Kluwer, 2001.

[16] G. Strang, *Linear Algebra and Its Applications*. Orlando, FL: Harcourt, 1988.

[17] M. Tesauro, P. Berardino, R. Lanari, E. Sansosti, G. Fornaro, and G. Franceschetti, "Urban subsidence inside the city of Napoli (Italy) observed by satellite radar interferometry," *Geophys. Res. Lett.*, vol. 27, no. 13, pp. 1961–1964, July 2000.

[18] R. Lanari, G. Zeni, M. Manunta, S. Guarino, P. Berardino, and E. Sansosti, "An integrated SAR/GIS approach for investigating urban deformation phenomena: The city of Napoli (Italy) case study," *Int. J. Remote Sens.*, vol. 25, no. 14, July 2004.

Riccardo Lanari (M'91–SM'01) received the laurea degree (summa cum laude) in electronic engineering from the University of Napoli "Federico II," Naples, Italy, in 1989.

He joined the Istituto per il Rilevamento Elettromagnetico dell'Ambiente (IREA), Italian National Council (CNR), Naples, in 1989, where he is currently a Senior Researcher and is also a member of the Institute Committee. He is an Adjunct Professor of electrical communications at the Università degli Studi del Sannio, Benevento, Italy, as well as a Lecturer of the SAR module course of the International Master in Airbone Photogrammetry and Remote Sensing, offered by the Institute of Geomatics in Barcelona. He was a Visiting Scientist at different foreign research institutes: ISAS (Japan, 1993), DLR (Germany, 1991 and 1994), and JPL (Pasadena, CA, 1997), where he also received a NASA recognition for the development of the ScanSAR processor used in the SRTM mission. His main research activities are in SAR data processing field and SAR interferometry techniques. On the latter topic, he has authored 30 international journal papers, and more recently, he coauthored the book *Synthetic Aperture Radar Processing* (Boca Raton, FL: CRC Press, 1999). He holds two patents on SAR data processing techniques.

Dr. Lanari has been invited as Chairman and Co-Chairman at several international conferences

Oscar Mora (M'98) received the electrical engineer degree from the Escola Tècnica Superior d'Enginyeria de Telecomunicació de Barcelona (ETSETB), Universitat Politècnica de Catalunya (UPC), Barcelona, Spain, in 1997.

He joined the Active Remote Sensing Group in 1999 in the framework of his Ph.D. work in the field of SAR differential interferometry. From September to December 2001, he was with the Istituto per il Rilevamento Elettromagnetico dell'Ambiente (IREA), Naples, Italy, in the frame of his Ph.D. work. His research is based on the study and development of new orbital SAR differential interferometric techniques for the monitoring of terrain surface displacements, such as the ones produced by volcanoes, earthquakes, or human activities. Recently, he joined the Institut Cartogràfic de Catalunya (ICC), Barcelona, Spain, for continuing his research activities in the field of SAR interferometry.

Michele Manunta was born in Cagliari, Italy, in 1975. He received the laurea degree in electronic engineering from the University of Cagliari, in 2001, with a thesis on synthetic aperture radar interferometry.

Since 2002, he has been with the Istituto per il Rilevamento Elettromagnetico dell'Ambiente (IREA), Italian National Research Council (CNR), Naples, Italy. His research interests are in the field of differential SAR interferometry and the SAR/GIS data integration. In particular, he studies deformations affecting both terrain surface (such as those produced by subsidence, volcano activity, and earthquake) and urban structures.

Jordi J. Mallorquí (S'90–M'96) was born in Tarragona, Spain, in 1966. He received the Ingeniero degree in telecommunication engineering and the Doctor Ingeniero degree in telecommunications engineering, in 1990 and 1995, respectively, both from the Universitat Politècnica de Catalunya (UPC), Barcelona, Spain.

In 1991, he joined the Department of Signal Theory and Communications as a Ph.D. student. In 1993, he became an Assistant Professor, and since 1997, he has been an Associate Professor at the Telecommunications Engineering School of UPC. His teaching activity involves microwaves, radio navigation, and remote sensing. He spent a sabbatical year at the Jet Propulsion Laboratory, Pasadena, CA, in 1999, working on interferometric airborne SAR calibration algorithms. He is currently working on the application of SAR interferometry to terrain subsidence monitoring with orbital and airborne data, vessel detection and classification from SAR images, and three-dimensional electromagnetic simulation of SAR systems. He has published more than 60 papers on microwave tomography, electromagnetic numerical simulation, SAR processing, interferometry, and differential interferometry.

Paolo Berardino (M'02) was born in Avellino, Italy, in 1971. He received the laurea degree in nautical sciences from the Naval University of Napoli, Naples, Italy, in 1998, with a thesis on synthetic aperture radar geocoding.

Since 1999, he has been with Istituto per il Rilevamento Elettromagnetico dell'Ambiente (IREA, formerly IRECE), Institute of the Italian National Research Council (CNR), Naples. His studies regard geocoding of SAR images and surface deformation observed by SAR interferometry (IFSAR). In particular, he applied the IFSAR technique in volcanic areas such as Mount Etna and Campi Flegrei for monitoring and modeling the deformation sources activity, and in the urban area of Naples to study the subsidence effects related to the underground excavations. He is currently working on a new approach for analyzing the temporal evolution of earth surface deformations based on the combination of DIFSAR interferograms.
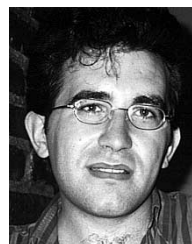
Eugenio Sansosti (M'98–SM'02) received the laurea degree (summa cum laude) in electronic engineering from the University of Napoli "Federico II," Naples, Italy, in 1995.

Since 1997, he has been with Istituto per il Rilevamento Elettromagnetico dell'Ambiente (IREA, formerly IRECE), Institute of the Italian National Research Council (CNR), Naples, Italy, where he is currently a Researcher. He is also an Adjunct Professor of Communications at University of Cassino, Cassino, Italy. He was Guest Scientist at the Jet Propulsion Laboratory, Pasadena, CA from August 1997 to February 1998, and again in February 2000, in support of the National Aeronautics and Space Administration Shuttle Radar Topography Mission. In November and December 2000, he worked as an Image Processing Adviser at the Istituto Tecnológico de Aeronáutica (ITA), São José dos Campos, São Paulo, Brazil. His main research interests are in airborne and spaceborne synthetic aperture radar (SAR) data processing, SAR interferometry, and differential SAR interferometry.